Nano Research Energy

ISSN 2791-0091 (print); 2790-8119 (online)
https://doi.org/10.26599/NRE.2026.9120241

Research Article

Evaporative/solar/thermal radiation regulations

Shancheng Wang[1,§], Ablimit Aili[2,§], Zhengui Zhou[1,§], Zhenqian Pang[2,3,§], Jianing Li[1], Haozhou Huang[2,3], Yan Cao[2,3], Gang Tan[3] (✉), and Yi Long[1] (✉)

[1] *Department of Electronic Engineering, The Chinese University of Hong Kong, New Territories, Hong Kong SAR, China*
[2] *Innovation Center of Yangtze River Delta, Zhejiang University, Jiashan 314100, China*
[3] *College of Civil Engineering and Architecture, Zhejiang University, Hangzhou 310000, China*
[§] *Shancheng Wang, Ablimit Aili, Zhengui Zhou, and Zhenqian Pang contributed equally to this work.*

Received: 16 April 2026 / **Revised:** 12 May 2026 / **Accepted:** 19 May 2026 / **Published date:** 24 June 2026

ABSTRACT

Buildings are estimated to account for approximately 40% of worldwide energy consumption. Dynamic outgoing thermal radiation modulation is an established technique for building thermal management, yet its performance is severely limited by its intrinsic power regulation capability and weather conditions. Theoretically, evaporative cooling (EC) could potentially offer one magnitude higher cooling power. However, the combined regulation of evaporation, outgoing thermal radiation, and solar transmittance for all weather conditions has not been investigated. This paper prototyped a design of triple evaporation/solar/thermal radiation regulative (TER) device which integrates an entangled smart hydrogel composite with a low-*E* overcoating, achieving a near unity dynamic regulation for evaporation (ΔE_{vap}, 93.2%), coupled with moderate solar and thermal radiation modulation. The reversible water retention/release mechanism of hydrogel was systematically elucidated by density function theory calculation, small-angle neutron scattering, and *ab initio* molecular dynamics calculations to understand the improved ΔE_{vap} due to entanglement. In simulations of an actual-sized building heating/cooling energy saving, this TER device displays a tripled annual heating/cooling energy saving compared with dual solar/thermal radiation regulative design (979 MJ vs. 276 MJ). This advancement in heat-regulative devices offers substantial potential for dynamic thermal management.

KEYWORDS

smart hydrogel, thermal management, evaporative cooling, entanglement, thermal radiation

1 Introduction

Reducing air-conditioning energy consumption in buildings is imperative in developing a sustainable globe. For example, in the building-densified regions, buildings consume 30% of the electricity that is mainly used for air-conditioning [1]. Window contributes to nearly 60% of energy losses due to their energy inefficiencies [2, 3].

By radiating heat through outgoing thermal radiation to cold outer space and reflecting sunlight to minimising heat gain, a surface can be spontaneously cooled down which is highly demanded in summer [4]. An ideal material should exhibit strong modulation capability in both summer and winter. Current material advancements offer potential solutions for dynamic outgoing thermal radiation regulation based on thermal [5–9], electrical [10–13], mechanical [14–16], and other stimuli [17, 18] (Table S1 in the Electronic Supplementary Material (ESM)). Yet, the existing state-of-the-art faces limitations due to low intrinsic cooling power modulations and its effectiveness fluctuates with the weather conditions. For example, in a cloudy condition, the intrinsic cooling power for outgoing thermal radiation will decrease significantly [19].

Evaporative cooling (EC) leverages water's large latent heat absorption during evaporation to provide cooling power [20–22]. EC has been investigated in personal heat management [23–27], electronic temperature control [28–30], and building thermal management [31–33] for cooling purposes due to its superior cooling power than solely relying on outgoing thermal radiation (theoretically up to 1000 W·m^{-2} vs. 100 W·m^{-2}) [21, 34, 35] (Table S2 in the ESM).

Therefore, the combined modulation of evaporation, thermal radiation, and solar transmittance is expected to give a stronger capability to manage the heat gain/heat loss across the building envelope. Herein, we prototype a passive triple evaporation/solar/thermal radiation regulative (TER) device, which autonomously modulates its evaporation, outgoing thermal radiation, and solar transmittance. This device integrates a thermal-responsive hydrogel composite with a spray coated low-*E* overcoating to adapt to different environmental temperatures passively. In winter, cooling is suppressed by the entangled water within the polymeric

Address correspondence to Gang Tan, tangang@zju.edu.cn; Yi Long, yilong@cuhk.edu.hk

matrix and exposed low-emission layer coupled with solar transparency. During summer, the entangled hydrogel undergoes phase separation, releasing water to the surface to give water evaporation with near-unity infrared emissivity and solar blockage due to the presence of free water and opacity. This tripled modulation of evaporation, outgoing thermal radiation, and solar transmittance results in a tripled annual heating/cooling energy saving compared with the existing dual solar/thermal radiation regulative design. The TER device's innovative design and functionality present a conceptual advancement in the field of heat modulation not limited to energy efficient buildings.

2 Design principle of TER smart device

The optimal water evaporation characteristics of TER device are displayed in Fig. 1(a). An ideal TER device should be responsive by enhancing water evaporation speed in summer and inhibiting water evaporation in winter. In detail, in summer, the water evaporation speed should be close to the theoretical maximum defined by the free water; while in winter, the water evaporation should be fully suppressed. To evaluate the efficacy of the TER, the theoretical monthly heat gain/loss densities of an ideal TER device and a dual solar/thermal radiation regulative device (marked as "DSR") were calculated in various climate conditions with distinct seasons (detailed calculations in Supplementary Note 1). In the cold winter and mild summer of Albuquerque (Fig. 1(b)), DSR device offers a moderate heat loss of ~60 W·m^{-2} in hot months due to its intrinsically limited outgoing thermal radiation capability but a promising heat gain of 953.1 W·m^{-2} in cold months. In comparison, the TER device shows a large heat loss of 767.2 W·m^{-2} during hot months and a promising heat gain in cold months. In the climates of Cairo (hot summer and mild winter, Fig. S1(a) in the ESM) and Perth (mild summer and mild winter, Fig. S1(b) in the ESM), TER device also shows promising hot season heat loss and cold season heat gain. The theoretical monthly heat gain/loss calculations demonstrate an enhanced year-round thermal management capability of TER by additional modulation of evaporation, coupled with conventional outgoing thermal radiation and solar transmittance regulations. The two major cooling components, outgoing thermal radiation ($P_{Broadband}$) and evaporation (P_{Evap}) of the devices for summer and winter are specifically analysed (Fig. 1(c)). In summer, the TER device achieves high $P_{Broadband-H}$ and P_{Evap-H} due to strong thermal radiation and evaporation. In winter, its $P_{Broadband-L}$ drops significantly to ~30 W·m^{-2}, while its P_{Evap-L} decreases to zero. These notable seasonal power density differences showcase the TER

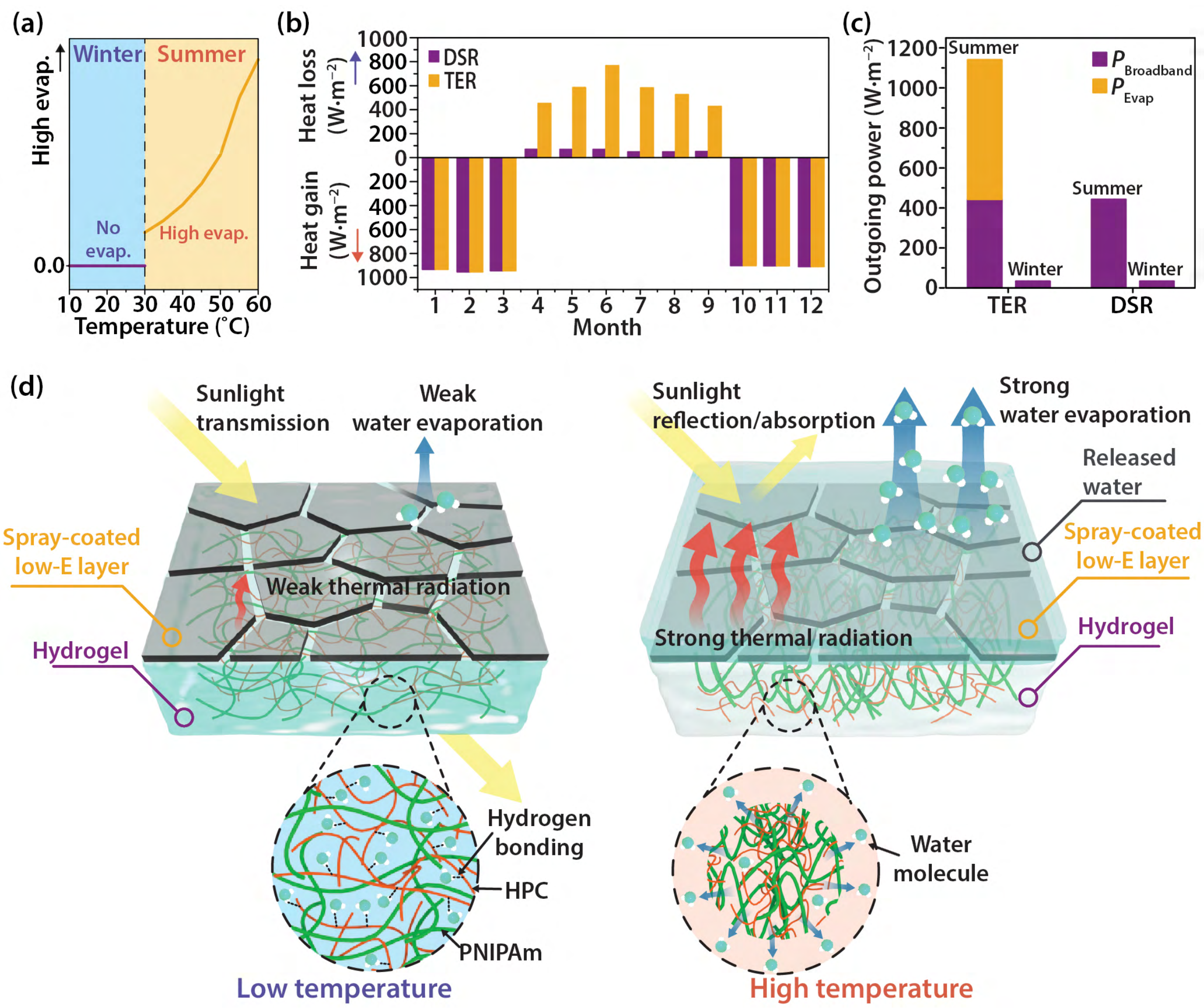

Figure 1 Theoretical design and scheme of TER smart device. (a) Concept of the ideal evaporation behaviour for energy saving TER device. The purple and yellow lines represent the ideal water evaporation speed for a TER device in winter and summer. A TER device should suppress its water evaporation in winter and promote its water evaporation in summer. (b) Theoretical monthly heat gain/loss calculation for TER device and DSR device. The unit of power density is W·m^{-2} regarding the device area. (c) Theoretical seasonal outgoing thermal radiation power ($P_{Broadband}$) and evaporation power (P_{Evap}) for TER and DSR, respectively. The power density of outgoing thermal radiation is not adjusted by atmospheric radiation. (d) Scheme of TER smart device at low and high temperatures.

device's robust thermal modulation ability to different seasons, which largely surpasses the dual solar/thermal radiation regulative design.

Guided by theoretical calculation, we prototyped TER smart device which involves thermal-responsive poly(N-isopropylacrylamide) (PNIPAm)-hydroxypropyl cellulose (HPC) entangled hydrogel and a spray-coated low-*E* overcoating that consists of $Ti_2C_3T_x$ MXene, silver nanowire (AgNWs), or copper nanowire (CuNWs) (Fig. 1(d)). The smart composite hydrogel is a key component of water evaporation regulation and solar modulation. At low temperatures, the hydrogel polymeric chain retains water molecules through hydrogen bonding effectively, facilitated by the HPC nanofiber entanglement in the composite, allowing for high solar transmittance (0.36–2.5 μm, T_{sol}) and minimal water evaporation. Spray-coated low-*E* layer exposed on the surface minimises the outgoing thermal radiation. As ambient temperatures rise, the hydrogel reaches its lower critical solution temperature (LCST) and prompts a structural and hydrophilicity/hydrophobicity change: It expels water through the entangled polymeric chain and the spaces between spray-coated low-*E* material clusters, leading to increased water evaporation and decreased T_{sol}, which in turn prevents solar heating and enhances cooling. Meanwhile, the water-covered TER device surface has a near-unity broadband IR emissivity (2.5–20 μm, $\varepsilon_{Broadband}$). The interplay between the hydrogel's capacity for water retention and release, combined with the low-*E* overcoating's thermal properties, realizes the triple regulation of water evaporation, outgoing thermal radiation, and solar transmittance autonomously in response to environmental temperature fluctuations passively.

3 Characterization of smart entangled hydrogel and MXene low-*E* coating

Figure 2(a) illustrates the photos of commonly used EC hydrogel polyacrylamide (PAAm) [20, 28] and our smart PNIPAm-HPC entangled hydrogel at different temperatures. At 25 °C, both hydrogels display promising transparency and allow clear views of the background image. When the temperature reaches above the PNIPAm-HPC entangled hydrogel's LCST (30 °C, Fig. S2 in the ESM), the entangled hydrogel becomes opaque while the PAAm remains transparent. The temperature-dependent optical properties of PAAm, PNIPAm, PNIPAm-HPC and PAAm-HPC were measured (Fig. S3 in the ESM). Different from PNIPAm and PNIPAm-HPC hydrogels, the PAAm and PAAm-HPC hydrogels are not responsive to temperature change.

The water evaporation performances of PNIPAm-HPC, PNIPAm, and conventional EC PAAm hydrogel were evaluated with the evaporation weight loss rate at different temperatures with the weight loss rate of free water as a comparison (Fig. 2(b), left). The smart PNIPAm-HPC and PNIPAm exhibit heightened evaporation rates increasing (0.05 $kg \cdot m^{-2} \cdot h^{-1} \cdot °C^{-1}$ from 30–60 °C) when the temperature exceeds 30 °C, while PAAm demonstrates a low temperature-sensitivity (0.02 $kg \cdot m^{-2} \cdot h^{-1} \cdot °C^{-1}$). Below LCST (Fig. 2(b), right, shaded in blue), PNIPAm-HPC entangled hydrogel exhibits more than 60% reduction in evaporation weight loss (0.06 $kg \cdot m^{-2} \cdot h^{-1}$) compared to free water (0.20 $kg \cdot m^{-2} \cdot h^{-1}$); and it is the minimal in three samples (0.07 $kg \cdot m^{-2} \cdot h^{-1}$ for PNIPAm and 0.08 $kg \cdot m^{-2} \cdot h^{-1}$ for PAAm at 25 °C, respectively). The relationship between HPC concentration and water evaporation speed in the entangled hydrogel, and the evaporation behaviour of the entangled hydrogel at low temperature are discussed in Supplementary Note 2 and Figs. S7 and S8 in the ESM, showing that with increasing HPC concentration, the evaporation rate decreases below LCST. Above the LCST, due to the hydrophilicity/hydrophobicity change of PNIPAm, a layer of free water is expelled from the hydrogel matrix and covers the hydrogel [36], and the evaporation rates across the sample with different HPC concentrations become similar. At low temperature, PNIPAm-HPC entangled hydrogel showed a lower evaporation weight loss than both free water and PAAm. A new performance index of evaporation rate modulation ability (ΔE_{vap}) is defined as the difference of evaporation rate between high and low temperature, normalized by the ideal case (Fig. 1(a), details in supplementary information "Materials and Method" session; ideal case is defined as zero evaporation at low temperature and same evaporation rate as free water at high temperature). The HPC entanglement further enhances the Δ*E*vap of smart hydrogel from 89.7% to 93.2%, which is more than doubled compared with the conventional EC PAAm (41.0%). The temperature-responsive water-releasing behaviour of PNIPAm-HPC entangled hydrogel is demonstrated in Fig. 2(c). At 25 °C, the water (stained in red for visualization) is well dispersed in the hydrogel. As the temperature rises across the LCST, the entangled hydrogel undergoes a significant volume contraction and free water is expelled to the surface, indicating the hydrogel's responsiveness to temperature and its phase separation. The SEM images of the entangled hydrogel across the LCST further show its temperature-induced morphological change (Fig. S9 in the ESM): At 25 °C, the polymer fibres are thin and elongated. When the temperature is above the LCST, the polymer fibres aggregate and the polymeric network collapses.

Density functional theory (DFT) simulation was used to understand the principle behind the HPC entanglement effects on the evaporation rate of the composite below its LCST (Supplementary Note 3 in the ESM). The charge density differences and their correlated Bader charge distributions were calculated for the DFT-optimized molecular structure (Fig. 2(d) and Fig. S10 in the ESM). The charge density changes due to the interaction among molecules are qualitatively represented by a light blue shade (representing a decrease in charge density) and a yellow shade (representing an increase in charge density), while Bader charge calculations quantify the charge changes that occurred in the systems. In the PNIPAm-water-HPC interaction scenario (Fig. 2(d), left), due to the introduction and entanglement of HPC, the electronegativities for two H and one O atoms in water are 0.64, 0.59, and −1.23, respectively. In contrast, for the PNIPAm-water interaction (Fig. 2(d), right), the electronegativities for two H and one O atoms in water are 0.60, 0.59, and −1.20, respectively. It can be noticed that the introduction of HPC alters the electronegativity of one of the H atoms in water from 0.60 to 0.64, which will strengthen the bonding between water and PNIPAm chains below the LCST. The binding energy simulations (Fig. 2(e)) for the two scenarios align with the Bader charge analysis. The PNIPAm-water-HPC system has a lower binding energy (−1 eV) compared with the interactions of PNIPAm-water (−0.24 eV). As the strong intermolecular attraction between water molecules and HPC could restrain water within the hydrogel below LCST [37, 38], HPC entanglement lowers the evaporation rate compared with pure PNIPAm (Fig. 2(b), right).

The structural difference between PNIPAm and PNIPAm-HPC entangled hydrogel, and their principle of temperature-responsive water-releasing behaviour were investigated and understood through temperature-dependent small-angle neutron scattering (SANS, Fig. 2(f), Supplementary Note 4 in the ESM). The freeze-

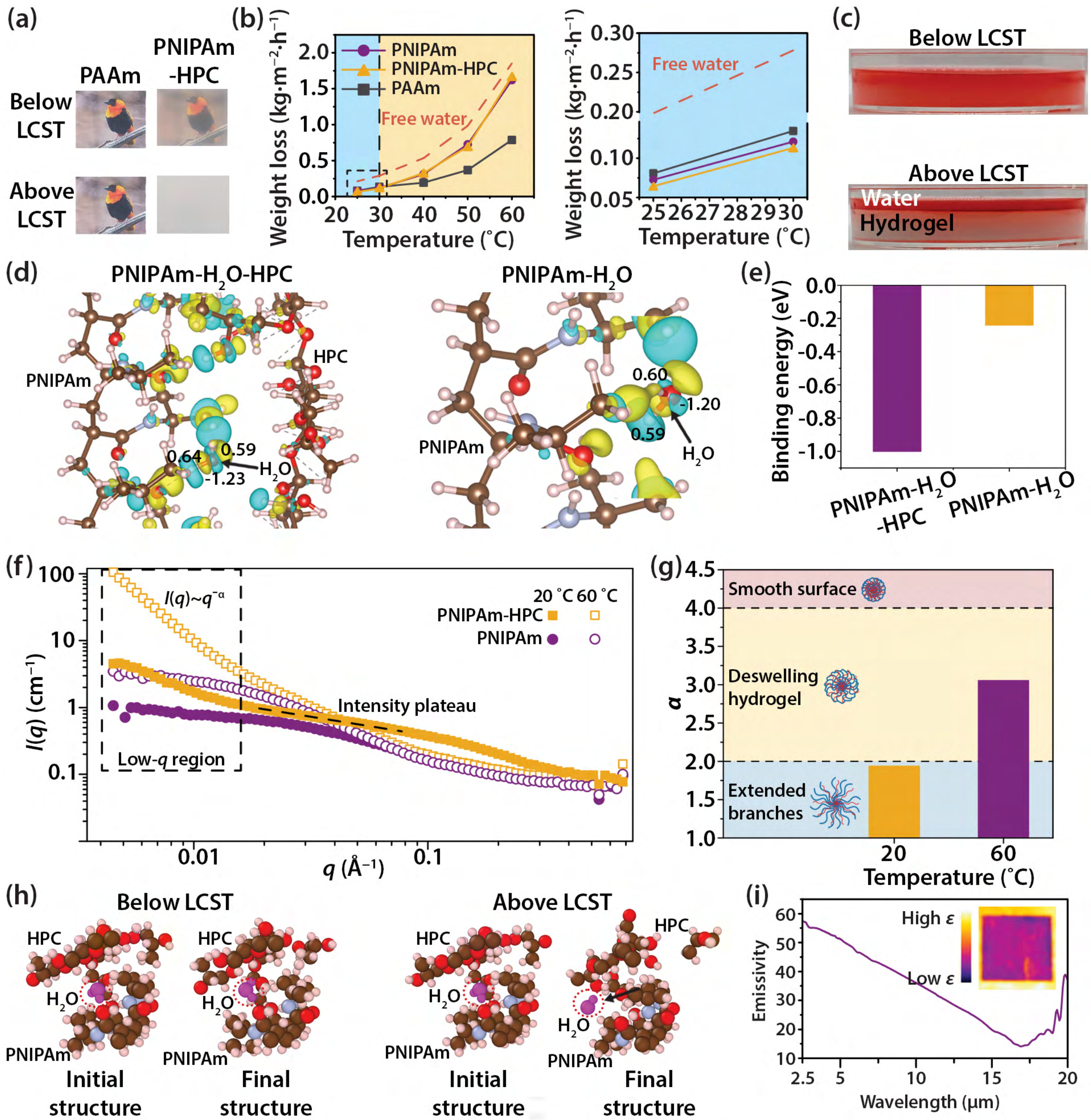

Figure 2 Characterization of smart hydrogel and MXene coatings. (a) Photos of PAAm and PNIPAm-HPC entangled hydrogel below and above LCST. (b) Left: Weight loss rates of PNIPAm, PNIPAm-HPC, and PAAm at variable temperatures from 25 to 60 °C. The red dashed line indicates the weight loss rate of free water. The blue shadow indicates the temperature range below the LCST. The yellow shadow indicates the temperature range above LCST. The dashed box represents the 25 to 30 °C region to be zoomed in. Right: Zoomed-in chart for weight losses of PNIPAm, PNIPAm-HPC, and PAAm at 25 to 30 °C. (c) Photos of red colour-stained water distribution in the entangled hydrogel below and above LCST. (d) Charge density difference and Bader charge distribution in the DFT-optimized molecular structures for left: PNIPAM-H_2O-HPC interaction and right: PNIPAm-H_2O interaction. Oxygen, carbon, and hydrogen atoms are represented with red, brown, and white beads, respectively. Light blue and yellow shades in the charge density represent the loss and gain of electrons, respectively. The isosurface is set as 0.001 e/Bohr³. (e) The simulated binding energy for interactions among PNIPAm-water-HPC and PNIPAm-water. (f) Temperature dependence SANS profiles for PNIPAm hydrogel and PNIPAm-HPC entangled hydrogel at 20 and 60 °C, respectively. The dashed box represents the low-q region used to analysis exponent α factor of PNIPAm-HPC entangled hydrogel. The dashed line highlights the intensity plateau presence in PNIPAm-HPC SANS profile at 20 °C. (g) Exponent α of PNIPAm-HPC at 20 and 60 °C and the hydrogel microgel structure with different exponent α factor, respectively. (h) The evolution of the PNIPAM-H_2O-HPC system undergoing relaxation below LCST (275 K, left) and above LCST (325 K, right), respectively. Water molecules are coloured purple and circled to indicate their motion. Oxygen, carbon, nitrogen, and hydrogen atoms are represented with red, brown, light blue, and light brown beads, respectively. (i) Emissivity curve of prepared MXene thin film. Inset: IR photo of MXene thin film. The surrounding yellow region is the background with an $\varepsilon_{Broadband}$ of 0.95.

dried hydrogels were dispersed into deuterium oxide (D_2O, heavy water), respectively, to form 5 wt.% PNIPAm and PNIPAm-HPC solutions. Both PNIPAm and PNIPAm-HPC showed distinct structural changes across the LCST. In particular, below the LCST at 20 °C, the scattered intensity $I(q)$ plateau in the scattering vector q range of 0.02–0.07 Å^{-1} is observed in the SANS profile of PNIPAm-HPC. The intensity plateau indicates that heavy water is well dispersed in the polymer matrix of the hydrogel [39]. Meanwhile, for the PNIPAm-HPC SANS profile above the LCST at 60 °C, the disappearance of the intensity plateau and the additional strong scattering for the low-q region (0.0045–0.015 Å^{-1}, highlighted by the dashed box) indicate the phase separation.

Meanwhile, although PNIPAm shows similar phase separation behaviour to PNIPAm-HPC entangled hydrogel, the low-q region curve upturn observed in the PNIPAm-HPC entangled hydrogel indicates a stronger structural inhomogeneity [40, 41], which may be due to the high density of entanglement in the hydrogel [42].

Moreover, the low-q region in PNIPAm-HPC SANS profiles was fitted by a decreasing power law $I(q)$~$q^{-\alpha}$. While the exponent factor α for PNIPAm-HPC at 20 and 60 °C was analysed as an indication of the surface condition of the hydrogel particles [43] (Fig. 2(g)). At 20 °C, the exponent factor α of hydrogel particles is ~2, which indicates that the polymer branches of hydrogel extend freely. With the temperature increases across the LCST, α of PNIPAm-HPC hydrogel particles increases to ~3. The increase of the exponent factor α reflects that the hydrogel particle is deswelling, its polymer chains experience collapsing and aggregation, and the phase separation between heavy water and polymer matrix happens. Moreover, we conducted *ab initio* molecular dynamics (MD) simulations for the PNIPAm-water-HPC primitive cells of the relaxed system under the constant temperature and volume (NVT) ensemble across LCST (Fig. 2(h)), respectively. Below the LCST at 275 K, atoms oscillate around their equilibrium positions, with the water molecule (circled in red) tightly bound to the system via hydrogen bonds (Fig. 2(h), left). Above the LCST at 325 K, with a 20% reduction of distance between the two ends of the chain, the polymer chains in the system shrink, and the water molecule is detached from the chain as indicated by the arrow in the figure (Fig. 2(h), right).

Through investigating the relationship between the layers of MXene coating and $\varepsilon_{Broadband}$ (Supplementary Note 5 in the ESM), the MXene thin film with 30 layers of coating was chosen for the fabrication of TER due to its lowest $\varepsilon_{Broadband}$ and acceptable T_{lum}. The MXene thin film's emissivity curve from 2.5 to 20 μm (Fig. 2(i)) reveals a low $\varepsilon_{Broadband}$ of 0.31, as visually corroborated by its homogenous purple hue against the bright yellow coloured high-E background ($\varepsilon_{Broadband}$: 0.95) in the IR camera image.

4 Performance evaluation of TER smart device

Figure 3(a) presents the UV-Vis-NIR spectra of the fabricated MXene-TER device prototype at 25 and 40 °C, respectively. The prototype shows a promising ΔT_{sol} of 17.1% due highly suppressed solar transmission at 40 °C, while still giving close to 20% T_{lum} at 25 °C. TER device's emissivity curve from 2.5 to 20 μm demonstrates a significant increase in $\varepsilon_{Broadband}$ with rising temperature (Fig. 3(b)), giving a promising $\Delta\varepsilon_{Broadband}$ of 0.38. To demonstrate TER's outgoing thermal radiation regulation ability, the inserted IR camera images were taken at 25 °C and 40 °C. At 25 °C, TER's lower-than-background emissivity indicates reduced thermal radiation and a darker colour under the IR camera than its surroundings. At 40 °C, the $\varepsilon_{Broadband}$ increases significantly to near-unity, and the IR photo is brighter than the background. The water evaporation properties of TER prototype were characterized and compared with the primitive PNIPAm-HPC hydrogel (Fig. 3(c)). At both 25°C (0.06 kg·m^{-2}·h^{-1} for both samples) and 60 °C (1.66 vs. 1.67 kg·m^{-2}·h^{-1}), the addition of MXene layers does not affect the EC. TER device prototype maintains a large ΔE_{vap} of 93.2% across the LCST. The evaporation, outgoing thermal radiation, and solar modulation abilities for TER, DSR smart window, and evaporative cooler are summarized in Fig. 3(d). Compared with the other designs, TER has outstanding performances in the first reported ΔE_{vap}, $\Delta\varepsilon_{Broadband}$, and ΔT_{sol}.

To evaluate the energy saving capability of TER, the solar and thermal management tests in controlled environments were conducted. In the hot environment test, TER, DSR window, and EC cooler were installed on the test chamber, and a solar simulator served as the light source. The ambient temperature was 24 °C. From the temperature curve, it can be observed that under constant sunlight irradiation, DSR window showed the most significant temperature increase and obtained a final temperature of 55.2 °C (Fig. 3(e)). In the meantime, the chamber with TER achieved the lowest temperature among the three samples at 27.6 °C. The hot environment solar/thermal management test shows that the TER possesses strong evaporation, strong outgoing thermal radiation, and low solar transmittance, which has a promising energy saving performance in a hot climate. Meanwhile, the cold climate energy-saving performance of TER was demonstrated by the solar and thermal management tests in the cold environment with an ambient temperature of 6.0 °C and a simulated sunlight source. Compared with the EC cooler without solar and thermal radiation regulation ability, TER showed a higher temperature (7.6 vs. 6.9 °C). These solar and thermal management tests show the promising energy-saving capability of TER. By combining the highly efficient hot environment indoor reduction (12.7 °C vs. the control) and promising cold environment warm keeping (1.6 °C higher than the ambient), TER showed good thermal management potential in both hot and cold environments. The outdoor field test for TER was conducted in Hong Kong with the DSR window and EC cooler as the benchmarks (Fig. 3(f), Fig. S15 in the ESM). Compared with the DSR window (52.3 °C) and EC cooler (43.8 °C), TER showed the lowest average temperature (39.6 °C) throughout the test (Fig. 3(g)). The outdoor test demonstrates the promising energy-saving performance of TER in the real-world application.

To further quantify the thermal management performance of the TER smart device, simulations of an actual-sized building heating/cooling energy consumption were conducted (Supplementary Note 6 in the ESM). The TER device was employed as a skylight. To simulate the application scenario in a region with distinct seasons, the climate data of Albuquerque, NM, US; Cairo, Egypt; Perth, WA, Australia [44] were applied. To comprehensively evaluate the TER smart device's energy efficiency, the performance of a DSR smart window [6] and a non-smart PAAm evaporative cooler were calculated as comparisons, with clear glass as the baseline. Figure 4(a) illustrates the energy saving performance of the TER smart skylight in different cities, which achieves the highest savings in annual heating and cooling energy compared with the DSR window and sole evaporative cooler. The TER smart skylight's ability to dynamically adjust to seasonal changes allows it to outperform the state of the art.

Moreover, Fig. 4(b) highlights the TER's promising power density regulation capabilities by showing ~80% seasonal modulation of evaporation power density (ΔP_{Evap}), 12.0% seasonal modulation of outgoing thermal radiation ($\Delta P_{Broadband}$), and 12.8% seasonal power density modulation of transmitted sunlight ($\Delta P_{in,sunlight}$). Meanwhile, the DSR window, while effective in ΔP_{LWIR} (23.2%), does not offer effective transmitted sunlight and evaporation control (3.6% for $\Delta P_{in,sunlight}$ and 0.0% for ΔP_{Evap}). Lastly, the evaporative cooler with no modulation functionality in evaporation, thermal radiation, and transmitted sunlight, is the least effective in achieving energy savings among the three candidates. The near-ideal evaporation regulation ability coupled with a moderate solar/thermal radiation regulation ability allows the TER device to effectively meet both summer cooling and

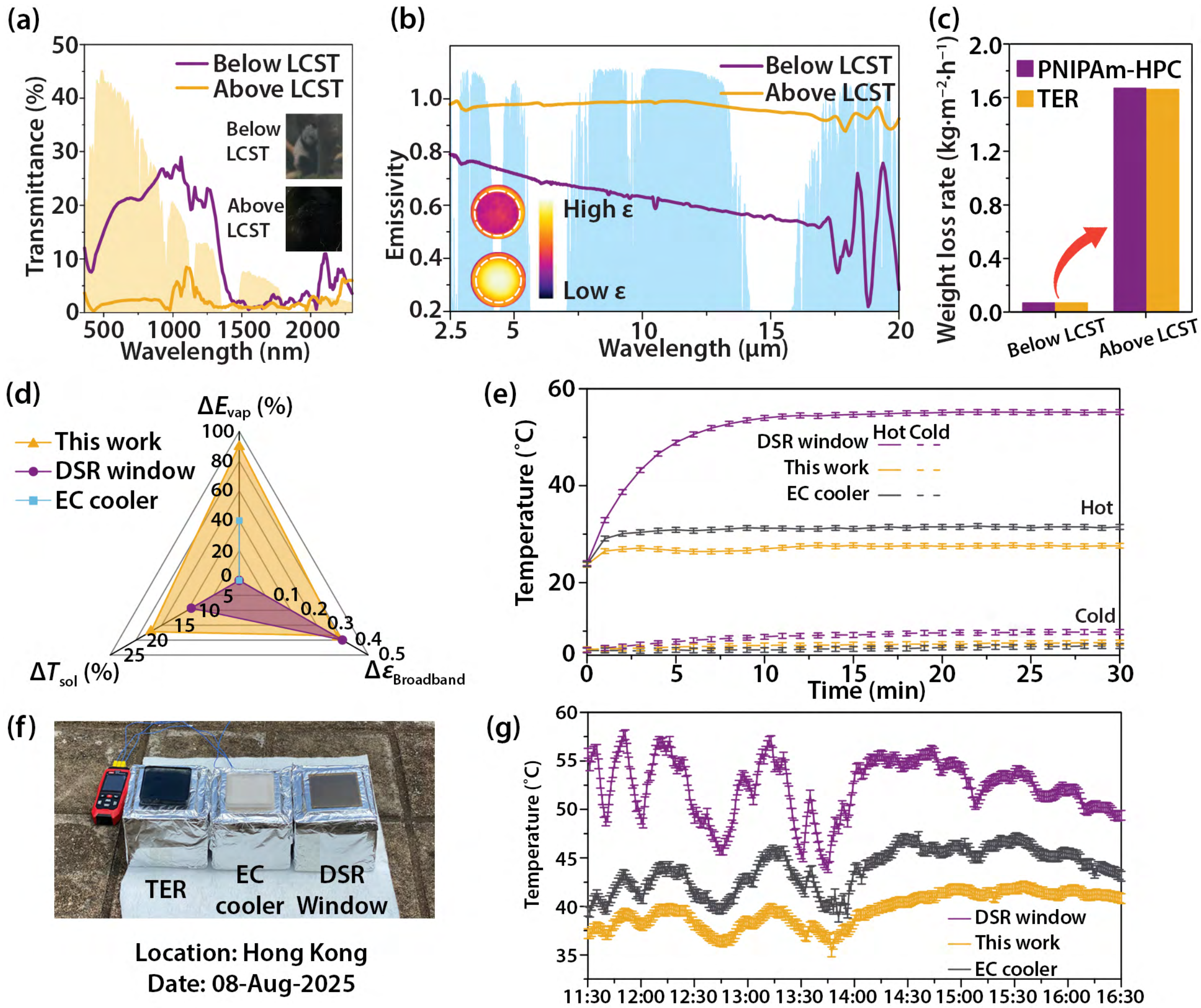

Figure 3 Performance evaluation and experimental validation for MXene-TER smart device. (a) UV-Vis-NIR spectra of TER device below and above LCST. The shadow in the background represents the AM 1.5 solar radiation spectrum. Inset: Photo of TER prototype across the LCST. (b) Emissivity curves of TER device across LCST below and above LCST. The shadow in the background represents the atmospheric transparency. Inset: IR photos of the TER device below and above the LCST. The samples are enclosed by dashed circles. The surrounding region is the background with an $\varepsilon_{\text{Broadband}}$ of 0.95. (c) Weight loss rates of PNIPAm-HPC and TER for the temperature below and above LCST. (d) Evaporation, outgoing thermal radiation, and solar modulation abilities summary for TER, DSR smart window [6], and evaporative cooler. The DSR smart window does not possess evaporation modulation abilities. The evaporative cooler does not possess outgoing thermal radiation and solar modulation abilities. (e) Temperature curves for TER, DSR window, and EC cooler in the solar and thermal management tests in the hot (solid line) and cold (dashed line) environment. (f) Photo of outdoors field test setup. The samples in the photo: left: TER; middle: EC cooler; right: DSR window. (g) Temperature curve in the field test for TER, EC cooler, and DSR window during the outdoor field test. The error bars for the temperature reading in (e) and (g) are ±0.5 °C due to the system error of the thermometer.

winter heating demands, making it highly suitable for climates like Albuquerque with significant seasonal variations.

The durability of TER was evaluated through a heating/cooling cycle test. The key performance indices, including visible transmittance (represented by transmittance @ 650 nm, Fig. 4(c)), emissivity (Fig. 4(d)), and weight loss rate (Fig. S16 in the ESM) were employed to assess the performance deterioration accompanied by the heating/cooling cycle. After 100 heating/cooling cycles, the three key performance indices showed less than 10% performance deterioration. The observations indicate that the TER has promising cyclability. To improve the applicability of TER for the real-world application scenario, a TER prototype with a water self-replenishment function was fabricated (Fig. 4(e)). The self-water replenish prototype consists of the hydrogel, a perforated holder, and the surrounding water reservoir made from the sponge (Fig. 4(f)). When the hydrogel is drying due to water evaporation, water will flow from the reservoir to the hydrogel through the perforated hole and keep the hydrogel moist. In order to visualise the water replenishment function of the design, an 18-hour water evaporation test was conducted (Fig. 4(g)). Compared with the control without the self-replenishment function, the hydrogel in the prototype shows a 24.3% less weight loss in a hot and dry environment (30 °C and 65%RH) due to the water replenishment from the reservoir. The water evaporation test demonstrates the efficacy of the self-replenishment design.

To demonstrate the applicability of the TER design, the TER with AgNWs and CuNWs as low-*E* overcoating was fabricated (Fig. 4(h)). The AgNWs-TER and CuNWs-TER demonstrate promising modulation abilities for evaporation, outgoing thermal, and solar transmittance (Table S7 in the ESM). Based on their optical properties and cost, MXene-TER, AgNWs-TER, and CuNWs-TER are suitable for different application scenarios. AgNWs-TER has the highest T_{lum} and is desired for applications requiring high daylight luminance and transparency, such as skylight. On the other hand, due to the best $\Delta\varepsilon_{\text{Broadband}}$ among the three designs, MXene-TER is suitable for the application required

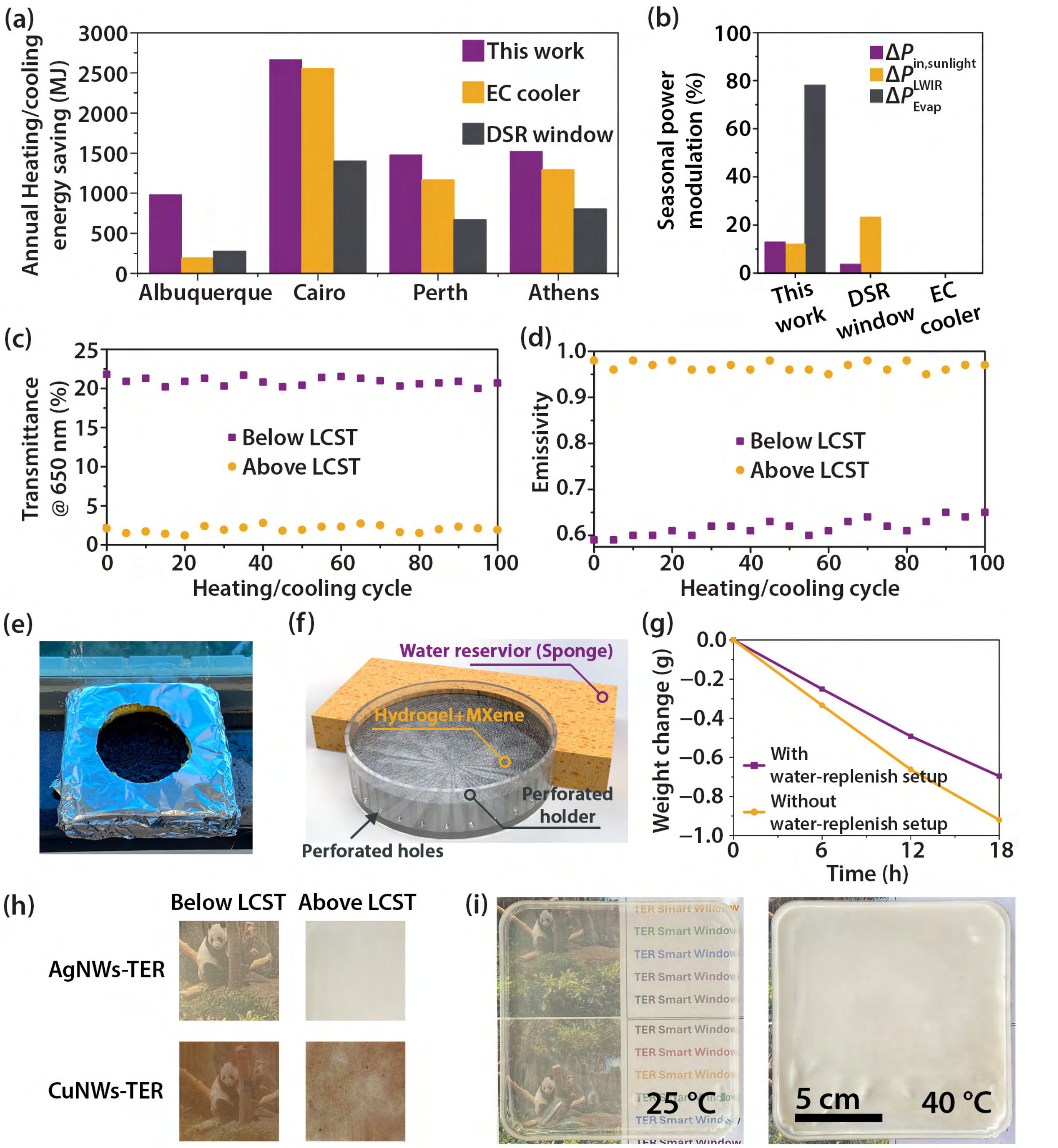

Figure 4 Energy simulation and applicability evaluation for TER smart device. (a) Annual heating/cooling energy saving simulation for TER, DSR smart window, and evaporative cooler in Albuquerque, Cairo, Perth, and Athens. The clear glass was selected as the baseline. (b) Seasonal power modulation abilities for TER, DSR smart window, and evaporative cooler in Albuquerque. The evaporative cooler does not possess seasonal power modulation abilities. (c) Transmittance @650nm below and above in the repeated heating/cooling cycle test. (d) Emissivity value across the LSCT in the repeated heating/cooling cycle test. (e) Photo of self-water replenish setup for TER. The water reservoir was covered by aluminium foil to minimise water evaporation. The TER sample is at the center of the setup. (f) Structural scheme of the self-water replenish setup. The water reservoir (the sponge) was cut in half to show the perforated hole on the holder. (g) Weight loss curve for the self-replenish setup and the control in the 18-hour water evaporation test. (h) Photos of AgNWs-TER and CuNWs-TER below and above the LCST, respectively. (i) Photos of large-scale (13 cm×13 cm) AgNWs-TER sample below and above the LCST.

high energy-saving. Lastly, as the CuNWs-TER has the lowest cost, it is preferred by large-scale, cost-sensitive applications. A 13 cm×13 cm AgNWs-TER sample was prepared to show the scalability of TER (Fig. 4(i)). The large-sized AgNWs-TER sample shows promising uniformity. When the ambient temperature is below the LCST, the large-sized sample shows promising transmittance. On the other hand, when the temperature is above the LCST, the large-sized sample becomes blocked.

5 Conclusion

In this paper, we reported a passive triple evaporation/solar/thermal radiation regulative (TER) device as the first instance to integrate evaporation, outgoing thermal radiation, and solar regulation in the pursuit of sustainable material for energy saving for all weather. Compared with the conventional dual solar/thermal radiation regulative design with limited thermal management capability, TER leverages the dynamic regulation of evaporation, outgoing thermal, and solar transmittance to provide enhanced modulation. The TER prototype possesses a near unity evaporation modulation (93.2%) with moderate and outgoing thermal radiation and solar regulation abilities (38% and 17.1% for LWIR emissivity and solar, respectively). In the simulations of actual-sized building heating/cooling energy saving, the TER boasts an impressive annual heating/cooling energy saving of 979 MJ, which is more than triple that of the dual solar/thermal radiation regulative (DSR) design. TER sets a new strategy for heat management design, and its promising performance in year-round thermal management highlights its potential, not limited to energy-efficient buildings.

6 Materials and methods

6.1 Materials

N-isopropylacrylamine (NIPAm, 98%, Sigma-Aldrich), hydroxypropyl cellulose (HPC, M_w=100,000, Aladdin), *N,N*-methylenebis(acrylamide) (BIS, crosslinker, 99%, Sigma-Aldrich), *N,N,N,N*-tetramethylethylenediamine (TEMED, accelerator, 99%, Sigma-Aldrich), ammonium peroxydisulfate (APS, initiator, 98%, Sigma-Aldrich), $Ti_2C_3T_x$ (MXene, Xinxi Technology), AgNWs (20 mg·mL^{-1}, dispersed in ethanol, XFNano), CuNWs (10 mg·mL^{-1}, dispersed in water, XFNano) Deuterium Oxide (D_2O, Aladdin) were used without further purification.

6.2 Preparation of HPC-PNIPAm composite hydrogel

1.13 g NIPAm, 16 mg BIS and variable amounts of HPC (0, 0.5, and 1 g for 0%, 5%, and 10% samples, respectively) were dissolved into 10 mL DI water at room temperature. The mixture was stirred at 1500 rpm for 30 min to obtain a homogeneous solution. Then, 60 μL 10 wt.% APS solution and 27 μL TEMED were added to the solution. The solution was stirred for 3 min at 1500 rpm. Finally, the prepared solution was poured into a mould. The mould and the solution were then put at 4 °C for 8 hours to obtain the final composite hydrogel.

6.3 Preparation of MXene-coated hydrogel for TER smart device

The purchased MXene was dispersed into DI water to form the MXene suspension with a concentration of 5 wt.%. The suspension was then ultrasonicated in an ice water bath for 30 min to ensure a good dispersion. The hydrogel was transferred into a perforated holder for constant water supply. After ultrasonication, the suspension was spray coated onto the surface of hydrogel with a hand-held spray gun (Eidolon JP 10, spray pressure: 30 PSI, nozzle size: 0.3 mm). The spray coating process was repeated 30 times with a coating time of 5 seconds for an individual spray. After each spray, the material was left exposed in the air for 2.5 min for drying.

6.4 Characterisation

The UV-Vis-NIR spectra for the samples were measured with a UV-Vis spectrometer system (AvaSpec-ULS2048L StarLine Versatile Fiber-optic Spectrometer and AvaSpec-NIR256-2.5-HSC-EVO, Avantes) with a heating/cooling stage (PE120, Linkam) equipped. The luminous transmittance (T_{lum}, 360–780 nm), and solar transmittance (T_{sol}, 250–2500 nm) were calculated by [45]

$$T_{\mathrm{lum/IR/sol}} = \int \varphi_{\mathrm{lum/sol}} T(\lambda)\,\mathrm{d}\lambda \int \varphi_{\mathrm{lum/sol}}\,\mathrm{d}\lambda \tag{1}$$

where $T(\lambda)$ is spectral transmittance, $\varphi_{lum}(\lambda)$ is the standard luminous efficiency function of photopic vision in the wavelength range of 360–780 nm [46]. On the other hand, $\varphi_{sol}(\lambda)$ is the solar irradiance spectrum for air mass 1.5 (corresponding to the sun standing 37° above the horizon with 1.5-atmosphere thickness, which corresponds to a solar zenith angle of 48.2°) [47].

The modulation ability ΔT was calculated by

$$\Delta T_{\mathrm{lum/sol}} = T_{\mathrm{lum/sol,cold}} - T_{\mathrm{lum/sol,hot}} \tag{2}$$

The emissivity curves of the samples were plotted based on Kirchhoff's law of thermal radiation: $\varepsilon(\lambda) = A(\lambda) = 1-T(\lambda)-R(\lambda)$ [48]. $R(\lambda)$ and $T(\lambda)$ are the spectral reflectance and the spectral transmittance that was measured by an FTIR spectrometer (Perkin Elmer Frontier) with an integration sphere and a self-designed heating stage attached. The integrated broadband emissivity $\varepsilon_{Broadband}$ was calculated by [48]

$$\varepsilon_{\mathrm{Broadband}} = \frac{\int_{2.5\,\mu\mathrm{m}}^{20\,\mu\mathrm{m}} I_{\mathrm{BB}}(T,\lambda)\,\varepsilon(T,\lambda)\,\mathrm{d}\lambda}{\int_{2.5\,\mu\mathrm{m}}^{20\,\mu\mathrm{m}} I_{\mathrm{BB}}(T,\lambda)\,\mathrm{d}\lambda} \tag{3}$$

where $I_{BB}(T, \lambda)$ is the spectral intensity emitted by a blackbody at temperature T and $\varepsilon(T, \lambda)$ is the surface's spectral hemispherical thermal emittance for the wavelength of 2.5–20 μm.

The water evaporation rates of the samples were measured in an environment with variable sample temperature and a constant relative humidity of 60%. The real-time weight change (Δm) of the samples was recorded by an electronic balance every 10 minutes for a continuous 60 minutes [49]. The water evaporation rate r is calculated by

$$r = \frac{\Delta m}{60} \tag{4}$$

The evaporation rate modulation ability ΔE_{vap} is calculated by

$$\Delta E_{\mathrm{vap}} = \frac{r_{\mathrm{H}} - r_{\mathrm{L}}}{r_{\mathrm{H,ideal}} - r_{\mathrm{L,ideal}}} \times 100\% \tag{5}$$

where r_H is the evaporation rate at 60 °C, and r_L is the evaporation rate at 25 °C. $r_{H,ideal}$ is the theoretical evaporation rate of water at 60 °C. While $r_{L,ideal}$ equals to 0 to represent the full inhibition of water evaporation below the LCST.

The theoretical evaporation rate of water is calculated by

$$r = \theta\left(\chi_{\mathrm{S}} - \chi\right) \tag{6}$$

where θ is the evaporation coefficient, which equals to 25+19v. v is the velocity of wind above the water surface. In the lab condition, v is considered as 0. X_S is the maximum humidity ratio of saturated air. While χ is the humidity ratio of ambient air.

SANS data were collected at the China Spallation Neutron Source (CSNS) using the BL01 beamline. The cold neutron flux had a wavelength range of 1–10 Å, and the q-range extended from 0.005 to 0.6 Å^{-1}. The resolution at q_{min} was approximately 35%. Data reduction included corrections for dark scattering using a boron nitride sheet at the sample position, cell scattering, D_2O scattering, and transmission. Standard software programs were used for data reduction. The contribution of the incoherent scattering due to hydrogen was also corrected by assuming the additivity of the incoherent scattering between PNIPAm-HPC and D_2O. The PNIPAm-HPC microgel particles were prepared by dispersing freeze-dried hydrogel in D_2O, the concentration of microgel solution was 5 wt.%. All samples were contained in 2-mm path length Hellma quartz cells, which were allowed to stabilise in the instrument's temperature-controlled chamber for 15 min prior to measurement.

The seasonal evaporation power density modulation ability ΔP_{Evap} is calculated by

$$\Delta P_{\text{Evap}} = \frac{P_{\text{Evap-H}} - P_{\text{Evap-L}}}{P_{\text{Evap,w-H}} - P_{\text{Evap,w-L}}} \times 100\% \tag{7}$$

where $P_{\text{Evap-H}}$ is the evaporation power density of the device in summer and $P_{\text{Evap-L}}$ is the evaporation power density of the device in winter. $P_{\text{Evap,w-H}}$ is the evaporation power density of water in summer and $P_{\text{Evap,w-L}}$ is the evaporation power density of water in winter.

The seasonal outgoing thermal radiation power density modulation ability $\Delta P_{\text{Broadband}}$ is calculated by

$$\Delta P_{\text{Broadband}} = \frac{P_{\text{Broadband-H}} - P_{\text{Broadband-L}}}{P_{\text{Broadband,Glass-H}} - P_{\text{Broadband,Glass-L}}} \times 100\% \tag{8}$$

where $P_{\text{Broadband-H}}$ is the outgoing thermal radiation power density of the device in summer and $P_{\text{Broadband-L}}$ is the outgoing thermal radiation power density of the device in winter; $P_{\text{Broadband,Glass-H}}$ is the outgoing thermal radiation power density of clear glass in summer and $P_{\text{Broadband,Glass-L}}$ is the outgoing thermal radiation power density of clear glass in winter.

The seasonal power density modulation ability for transmitted sunlight $\Delta P_{\text{in,sunlight}}$ is calculated by

$$\Delta P_{\text{in,sunlight}} = \frac{P_{\text{in,sunlight-H}} - P_{\text{in,sunlight-L}}}{P_{\text{in,sunlight,Glass-H}} - P_{\text{in,sunlight,Glass-L}}} \times 100\% \tag{9}$$

where $P_{\text{in,sunlight-H}}$ is the transmitted sunlight power density of the device in summer and $P_{\text{in,sunlight-L}}$ is the transmitted sunlight power density of the device in winter; $P_{\text{in,sunlight,Glass-H}}$ is the transmitted sunlight power density of clear glass in summer and $P_{\text{in,sunlight,Glass-L}}$ is the transmitted sunlight power density of clear glass in winter.

Acknowledgements

Y.L. is thankful for the funding support from the Global STEM Professorship Scheme sponsored by the Government of Hong Kong Special Administrative Region, Start-up funding from The Chinese University of Hong Kong, 2024 Shenzhen-Hong Kong-Macau Science and Technology Program (Category C) (SGDX20230821094659005), and Innovation and Technology Fund (ITS/221/23). G.T. is thankful for the funding support from National Key Research and Development Program of China (No. 2023YFC3806300). Z.P. is thankful for the funding support from National Natural Science Foundation of China (NSFC, No. 12302143). The DFT computations in this paper were run on the cluster supported by the High-Performance Computing at the Innovation Center of Yangtze River Delta, Zhejiang University. The authors would like to thank the support from China Spallation Neutron Source (CSNS) the access to SANS beamlines (BL-01).

Author contributions:

Conceptualization: Y.L.; Methodology: Y.L., G.T., S.W., A.A., Z.Z., Z.P., J.L., H.H., Y.C.; Investigation: S.W., A.A., Z.Z., Z.P., J.L.; Visualization: S.W., Z.P.; Funding acquisition: Y.L., G.T.; Project administration: Y.L., G.T.; Supervision: Y.L., G.T.; Writing – original draft: S.W., A.A., Z.Z., Z.P.; Writing – review & editing: Y.L., G.T.

Declaration of conflicting interests

The authors declare no conflicting interests regarding the content of this article. A U.S. provisional patent (No.: 63/553,815) related to this work has been filed by Y.L., S.W., and Z.Z..

Data availability

All data needed to support the conclusions in the paper are presented in the manuscript and/or the Supplementary Materials. Additional data related to this paper may be requested from the corresponding author upon request.

Electronic Supplementary Material: Supplementary material (calculation details of theoretical heat gain/heat loss, additional simulation details about DFT, MD simulation, and actual-sized building heating/cooling, cost estimation for TER, and additional details for the characterization of MXene/AgNWs/CuNWs-TER) is available in the online version of this article at https://doi.org/10.26599/NRE.2026.9120241.

References

[1] EMSD. Hong Kong Energy End-use Data 2023. Hong Kong SAR Government; Hong Kong SAR, 2023.
[2] Hee, W. J.; Alghoul, M. A.; Bakhtyar, B.; Elayeb, O.; Shameri, M. A.; Alrubaih, M. S.; Sopian, K. The role of window glazing on daylighting and energy saving in buildings. *Renew. Sustain. Energy Rev.* **2015**, *42*, 323–343.
[3] Lee, E. S.; Pang, X. F.; Hoffmann, S.; Goudey, H.; Thanachareonkit, A. An empirical study of a full-scale polymer thermochromic window and its implications on material science development objectives. *Sol. Energy Mater. Sol. Cells* **2013**, *116*, 14–26.
[4] Yin, X. B.; Yang, R. G.; Tan, G.; Fan, S. H. Terrestrial radiative cooling: Using the cold universe as a renewable and sustainable energy source. *Science* **2020**, *370*, 786–791.
[5] Tang, K. C.; Dong, K. C.; Li, J. C.; Gordon, M. P.; Reichertz, F. G.; Kim, H.; Rho, Y.; Wang, Q. J.; Lin, C. Y.; Grigoropoulos, C. P. et al. Temperature-adaptive radiative coating for all-season household thermal regulation. *Science* **2021**, *374*, 1504–1509.
[6] Wang, S. C.; Jiang, T. Y.; Meng, Y.; Yang, R. G.; Tan, G.; Long, Y. Scalable thermochromic smart windows with passive radiative cooling regulation. *Science* **2021**, *374*, 1501–1504.
[7] Ao, X. Z.; Li, B. W.; Zhao, B.; Hu, M. K.; Ren, H.; Yang, H. L.; Liu, J.; Cao, J. Y.; Feng, J. S.; Yang, Y. J. et al. Self-adaptive integration of photothermal and radiative cooling for continuous energy harvesting from the sun and outer space. *Proc. Natl. Acad. Sci. USA* **2022**, *119*, e2120557119.
[8] Zhang, Q.; Wang, Y. F.; Lv, Y. W.; Yu, S. X.; Ma, R. J. Bioinspired zero-energy thermal-management device based on visible and infrared thermochromism for all-season energy saving. *Proc. Natl. Acad. Sci. USA* **2022**, *119*, e2207353119.
[9] Lin, C. J.; Hur, J.; Chao, C. Y. H.; Liu, G. Z.; Yao, S. H.; Li, W. H.; Huang, B. L. All-weather thermochromic windows for synchronous solar and thermal radiation regulation. *Sci. Adv.* **2022**, *8*, eabn7359.
[10] Li, M. Y.; Liu, D. Q.; Cheng, H. F.; Peng, L.; Zu, M. Manipulating metals for adaptive thermal camouflage. *Sci. Adv.* **2020**, *6*, eaba3494.
[11] Rao, Y. F.; Dai, J. Y.; Sui, C.; Lai, Y. T.; Li, Z.; Fang, H. M.; Li, X. Q.; Li, W.; Hsu, P. C. Ultra-wideband transparent conductive electrode for electrochromic synergistic solar and radiative heat management. *ACS Energy Lett.* **2021**, *6*, 3906–3915.
[12] Banerjee, D.; Hallberg, T.; Chen, S. Z.; Kuang, C. Y.; Liao, M. N.; Kariis, H.; Jonsson, M. P. Electrical tuning of radiative cooling at ambient conditions. *Cell Rep. Phys. Sci.* **2023**, *4*, 101274.
[13] Mandal, J.; Du, S. C.; Dontigny, M.; Zaghib, K.; Yu, N.; Yang, Y. $Li_4Ti_5O_{12}$: A visible-to-infrared broadband electrochromic material

for optical and thermal management. *Adv. Funct. Mater.* **2018**, *28*, 1802180.
[14] Xu, C. Y.; Stiubianu, G. T.; Gorodetsky, A. A. Adaptive infrared-reflecting systems inspired by cephalopods. *Science* **2018**, *359*, 1495–1500.
[15] Leung, E. M.; Colorado Escobar, M.; Stiubianu, G. T.; Jim, S. R.; Vyatskikh, A. L.; Feng, Z. J.; Garner, N.; Patel, P.; Naughton, K. L.; Follador, M. et al. A dynamic thermoregulatory material inspired by squid skin. *Nat. Commun.* **2019**, *10*, 1947.
[16] Wang, S. C.; Dong, Y. T.; Li, Y. B.; Ryu, K.; Dong, Z. L.; Chen, J.; Dai, Z. D.; Ke, Y. J.; Yin, J.; Long, Y. Solar/radiative cooling dual-regulation smart window based on shape-morphing kirigami structures. *Mater. Horiz.* **2023**, *10*, 4243–4250.
[17] Li, X. Q.; Sun, B. W.; Sui, C.; Nandi, A.; Fang, H. M.; Peng, Y. C.; Tan, G.; Hsu, P. C. Integration of daytime radiative cooling and solar heating for year-round energy saving in buildings. *Nat. Commun.* **2020**, *11*, 6101.
[18] Wang, S. C.; Zhou, Y.; Jiang, T. Y.; Yang, R. G.; Tan, G.; Long, Y. Thermochromic smart windows with highly regulated radiative cooling and solar transmission. *Nano Energy* **2021**, *89*, 106440.
[19] Zhao, D. L.; Aili, A.; Zhai, Y.; Xu, S. Y.; Tan, G.; Yin, X. B.; Yang, R. G. Radiative sky cooling: Fundamental principles, materials, and applications. *Appl. Phys. Rev.* **2019**, *6*, 021306.
[20] Lu, Z. M.; Strobach, E.; Chen, N. X.; Ferralis, N.; Grossman, J. C. Passive sub-ambient cooling from a transparent evaporation-insulation bilayer. *Joule* **2020**, *4*, 2693–2701.
[21] Li, J. L.; Wang, X. Y.; Liang, D.; Xu, N.; Zhu, B.; Li, W.; Yao, P. C.; Jiang, Y.; Min, X. Z.; Huang, Z. Z. et al. A tandem radiative/evaporative cooler for weather-insensitive and high-performance daytime passive cooling. *Sci. Adv.* **2022**, *8*, eabq0411.
[22] Chen, X. Y.; Ye, Q.; Shi, C. M.; Zhang, L. W.; Zhou, P.; Chen, M. J. Understanding solar thermal gradient to improve solar evaporation performance for water collection. *Nano Res. Energy* **2025**, *4*, e9120152.
[23] Fang, Y. S.; Zhao, X.; Chen, G. R.; Tat, T.; Chen, J. Smart polyethylene textiles for radiative and evaporative cooling. *Joule* **2021**, *5*, 752–754.
[24] Zhang, X. S.; Yang, W. F.; Shao, Z. W.; Li, Y. G.; Su, Y.; Zhang, Q. H.; Hou, C. Y.; Wang, H. Z. A moisture-wicking passive radiative cooling hierarchical metafabric. *ACS Nano* **2022**, *16*, 2188–2197.
[25] Alberghini, M.; Hong, S.; Lozano, L. M.; Korolovych, V.; Huang, Y.; Signorato, F.; Zandavi, S. H.; Fucetola, C.; Uluturk, I.; Tolstorukov, M. Y. et al. Sustainable polyethylene fabrics with engineered moisture transport for passive cooling. *Nat. Sustain.* **2021**, *4*, 715–724.
[26] Hu, X. Y.; Hu, P. Y.; Liu, L.; Zhao, L. M.; Dou, S. Y.; Lv, W. B.; Long, Y.; Wang, J.; Li, Q. W. Lightweight and hierarchically porous hydrogels for wearable passive cooling under extreme heat stress. *Matter* **2024**, *7*, 4398–4409.
[27] Yao, H. Z.; Cheng, H. H.; Liao, Q. H.; Hao, X. Z.; Zhu, K. X.; Hu, Y. J.; Qu, L. T. Integrated radiative and evaporative cooling beyond daytime passive cooling power limit. *Nano Res. Energy* **2023**, *2*, e9120060.
[28] Pu, S. R.; Fu, J.; Liao, Y. T.; Ge, L. R.; Zhou, Y. H.; Zhang, S. L.; Zhao, S. L.; Liu, X. W.; Hu, X. J.; Liu, K. et al. Promoting energy efficiency via a self-adaptive evaporative cooling hydrogel. *Adv. Mater.* **2020**, *32*, 1907307.
[29] Mu, X. J.; Shi, X. L.; Zhou, J. H.; Chen, H.; Yang, T. T.; Wang, Y. T.; Miao, L.; Chen, Z. G. Self-hygroscopic and smart color-changing hydrogels as coolers for improving energy conversion efficiency of electronics. *Nano Energy* **2023**, *108*, 108177.
[30] Shi, P. R.; Li, Y. Z.; Liu, G. L.; Zeng, M. Y.; Wang, J. Y.; Zhou, L.; Zhu, J.; Xu, N. Fluoroelastomer-engineered atmospheric hygroscopic hydrogels with adhesive and anticorrosive interfaces for efficient and stable evaporative cooling. *Adv. Funct. Mater.* **2026**, *36*, e31131.
[31] Feng, C. Z.; Yang, P. H.; Liu, H. D.; Mao, M. R.; Liu, Y. P.; Xue, T.; Fu, J.; Cheng, T.; Hu, X. J.; Fan, H. J. et al. Bilayer porous polymer for efficient passive building cooling. *Nano Energy* **2021**, *85*, 105971.
[32] Fei, J. P.; Zhang, X.; Han, D.; Lei, Y.; Xie, F.; Zhou, K.; Koh, S. W.; Ge, J. Y.; Zhou, H.; Wang, X. L. et al. Passive cooling paint enabled by rational design of thermal-optical and mass transfer properties. *Science* **2025**, *388*, 1044–1049.
[33] Yin, B.; Xiong, Z. C.; Chen, H. Y.; Poredoš, P.; Wang, R. Z.; Li, T. X.; Xu, J. X. Passive isothermal film enabled by synergistic sky radiation energy harvesting and storage. *Nano Res. Energy* **2024**, *3*, e9120145.
[34] Aili, A.; Yin, X. B.; Yang, R. G. Passive sub-ambient cooling: Radiative cooling versus evaporative cooling. *Appl. Therm. Eng.* **2022**, *202*, 117909.
[35] Yu, L.; Huang, Y. M.; Li, W. H.; Shi, C. M.; Sheldon, B. W.; Chen, Z.; Chen, M. J. Radiative-coupled evaporative cooling: Fundamentals, development, and applications. *Nano Res. Energy* **2024**, *3*, e9120107.
[36] Zhong, Y. T.; Fang, Z.; Cao, B. Y.; Wu, S. G.; Fan, X. C.; Xia, Z. L. An adaptive direct evaporative cooler that regulates the sub-ambient temperature by controlling the evaporation rate. *J. Therm. Sci. Eng. Appl.* **2023**, *15*, 051004.
[37] Guo, Y. H.; Guan, W. X.; Lei, C. X.; Lu, H. Y.; Shi, W.; Yu, G. H. Scalable super hygroscopic polymer films for sustainable moisture harvesting in arid environments. *Nat. Commun.* **2022**, *13*, 2761.
[38] Feng, Y. Q.; Wang, S. C.; Li, Y. Q.; Ma, W. X.; Zhang, G.; Yang, M.; Li, H. B.; Yang, Y. S.; Long, Y. Entanglement in smart hydrogels: Fast response time, anti-freezing and anti-drying. *Adv. Funct. Mater.* **2023**, *33*, 2211027.
[39] Nishi, K.; Hiroi, T.; Hashimoto, K.; Fujii, K.; Han, Y. S.; Kim, T. H.; Katsumoto, Y.; Shibayama, M. SANS and DLS study of tacticity effects on hydrophobicity and phase separation of poly(*N*-isopropylacrylamide). *Macromolecules* **2013**, *46*, 6225–6232.
[40] Dai, W. T.; Xie, Z. H.; Ke, Y. B.; You, Y.; Zhang, Z. P.; Rong, M. Z.; Zhang, M. Q. Microstructural convergence of subnetworks in reversibly interlocked polymer networks revealed by small-angle neutron scattering. *Macromolecules* **2025**, *58*, 5145–5152.
[41] Matsunaga, T.; Sakai, T.; Akagi, Y.; Chung, U. I.; Shibayama, M. SANS and SLS studies on tetra-arm PEG gels in As-prepared and swollen states. *Macromolecules* **2009**, *42*, 42–6252.
[42] Saffer, E. M.; Lackey, M. A.; Griffin, D. M.; Kishore, S.; Tew, G. N.; Bhatia, S. R. SANS study of highly resilient poly(ethylene glycol) hydrogels. *Soft Matter* **2014**, **10**, 1905–1916.
[43] Fernández-Barbero, A.; Fernández-Nieves, A.; Grillo, I.; López-Cabarcos, E. Structural modifications in the swelling of inhomogeneous microgels by light and neutron scattering. *Phys. Rev. E* **2002**, *66*, 051803.
[44] ANSI/ASHRAE/IES Energy standard for building except low-rise residential buildings. 2016.
[45] Wang, S. C.; Liu, G. W.; Hu, P.; Zhou, Y.; Ke, Y. J.; Li, C. C.; Chen, J.; Cao, T.; Long, Y. Largely lowered transition temperature of a VO_2/carbon hybrid phase change material with high thermal emissivity switching ability and near infrared regulations. *Adv. Mater. Interfaces* **2018**, *5*, 1801063.
[46] Wyszecki, G.; Stiles, W. S. *Color Science: Concepts and Methods, Quantitative Data and Formulae*; 2nd ed. Wiley: New York, 2000.
[47] ASTM ASTM G173-03 Standard tables for reference solar spectral irradiances: Direct normal and hemispherical on 37° tilted surface. American Society for Testing and Materials: Philadelphia, PA, USA, 2012.
[48] Ke, Y. J.; Li, Y. B.; Wu, L. C.; Wang, S. C.; Yang, R. G.; Yin, J.; Tan, G.; Long, Y. On-demand solar and thermal radiation management based on switchable interwoven surfaces. *ACS Energy Lett.* **2022**, *7*, 1758–1763.
[49] Wang, Y. D.; Hu, J. Q.; Yu, L.; Wu, X.; Zhang, Y. Y.; Xu, H. L. Recent strategies for constructing efficient interfacial solar evaporation systems. *Nano Res. Energy* **2023**, *2*, e9120062.

Shancheng Wang received his BEng and PhD degrees from Nanyang Technological University, Singapore, in 2016 and 2021, respectively. From 2021 to 2023, he conducted postdoctoral research at Nanyang Technological University. From 2023 to 2025, he was a postdoctoral researcher at The Chinese University of Hong Kong. Currently, he is an assistant professor in the Department of Physics, Hong Kong Baptist University. His research interests focus on the development of phase change hydrogels for sustainable applications.

Ablimit Aili is currently a Research Scientist at the Innovation Center of Yangtze River Delta, Zhejiang University. He received his PhD in Mechanical Engineering from the University of Colorado Boulder, and previously held the Presidential Postdoctoral Fellowship at Nanyang Technological University, Singapore. His research spans thermal sciences and its applications in green and smart buildings, green data centers, and smart renewable micro-grids. He has authored over 20 papers in leading international journals including Nature Electronics, Joule, and Applied Energy.

Zhengui Zhou is currently a postdoc researcher in the Department of Electronic Engineering, The Chinese University of Hong Kong. Prior to joining CUHK, he held the position of research fellow at Nanyang Technological University. He received his Ph.D. from Huazhong University of Science and Technology, China. His ongoing research centers on energy-saving windows, smart devices, and thermal management techniques.

Zhenqian Pang is a Professor at the College of Civil Engineering and Architecture, Zhejiang University. He received his Ph.D. in Solid Mechanics from the Institute of Mechanics, Chinese Academy of Sciences, and conducted postdoctoral research at the University of Maryland. His research focuses on multiscale mechanics, microstructured functional materials, and high-performance biomaterials.

Gang Tan is a currently a distinguished Qiushi Chair Professor at the College of Civil Engineering and Architecture, Zhejiang University. His research interests include new building materials, new technologies for energy conservation and emission reduction, renewable energy and utilization, and building environment control. He received his Ph.D. in building technology from Massachusetts Institute of Technology in 2005. Prior to joining Zhejiang University in 2022, he worked at the University of Wyoming in the United States and was awarded a tenured professor position. He has published about 100 research papers in prestigious research journals, including Science (3 papers), Joule, Nature Communications, ACS Energy Letters.

Yi Long is a full professor at the Department of Electronic Engineering, The Chinese University of Hong Kong (CUHK). Her major research includes smart surfaces for energy saving, flexible devices, soft electronics, and nanodevice fabrications. She received her Ph.D. degree in Materials Science from Cambridge University, United Kingdom, in 2005 under full sponsorship of Overseas Research Scholarship (ORS), United Kingdom, Cambridge Trust, and Graduate Scholarship of Selwyn College. Before joining CUHK, she worked at Nanyang Technological University as a faculty member from 2005 to 2022. She is currently a Fellow of the Royal Society of Chemistry.